Int. J. Heat Mass Transfer. Vol. 33, No. 10, pp. 2089–2098, 1990
Printed in Great Britain

0017-9310/90 $3.00 + 0.00

Heat transfer and fluid flow in welding arcs produced by sharpened and flat electrodes

M. C. TSAI and SINDO KOU
Center of Excellence in Solidification Processing Technologies of Engineering Materials, and Department of Materials Science and Engineering, University of Wisconsin, Madison, WI 53706, U.S.A.

(*Received* 8 *February* 1989 *and in final form* 30 *November* 1989)

Abstract—A steady-state, two-dimensional model is developed to describe heat transfer and fluid flow in gas-tungsten welding arcs. The model differs from the previous ones in that it considers the electrode tip geometry, the arc length realistic for welding, and the presence of the shielding-gas nozzle. The effects of the electrode tip geometry on the following items are demonstrated using the model: the distributions of the current density, electromagnetic force, velocity and temperature in the arc plasma, the arc shape and the arc pressure. The calculated temperature distributions in the arc plasma and maximum arc pressure at the anode are compared with existing experimental data.

INTRODUCTION

A SCHEMATIC sketch of the so-called gas-tungsten arc (GTA) welding process [1] is shown in Fig. 1, along with the commonly used terminology. The cathode is a tungsten electrode, usually doped with 2% thoria to help thermionic emission of electrons, while the anode is the workpiece being welded. However, in most experimental or theoretical studies of the arc plasma, as in the present case, the anode is a copper plate water-cooled to prevent melting, so that a stationary axisymmetrical arc can be established. The ceramic nozzle surrounding the electrode helps direct the shielding gas toward the anode, which usually is pure Ar but can also be other gases. The arc consists of both heavy particles, i.e. ions and neutral atoms of the shielding gas, and electrons. It can be separated into three different regions, i.e. the cathode region immediately adjacent to the cathode surface, the arc plasma, and the anode region immediately adjacent to the anode surface. The electrode regions are of the order of 0.1 mm thick, while the arc plasma, which is the main body of the arc, is of the order of 1–3 mm long under normal GTA welding conditions (i.e. up to about 250 A welding current).

The study of heat transfer and fluid flow in the weld pool, especially in the GTA weld pool, has been an area of active research in recent years, and it is now well recognized that fluid mechanical and heat transfer considerations can significantly affect the shape, microstructure and mechanical properties of the resultant weld (e.g. ref. [2]). The study of heat transfer and fluid flow in the welding arc is equally important, since they can significantly affect heat transfer and fluid flow in the weld pool.

In modeling heat transfer and fluid flow in the weld pool, the calculation of the electromagnetic force can be decoupled from that of heat transfer and fluid flow, since the latter two do not significantly affect the former. This, however, is not true in modeling heat transfer and fluid flow in the welding arc. For instance, since the degree of ionization and hence the electrical conductivity of the arc plasma are temperature dependent, the calculation of the current density vector and hence the electromagnetic force has to be coupled with that of heat transfer and fluid flow.

Modeling heat transfer and fluid flow in the arc plasma, with truly coupled electromagnetic force, heat transfer and fluid flow, has not been carried out until recently by Hsu *et al.* [3], and subsequently by McKelliget and Szekely [4] and Kovitya and Cram [5]. These studies all dealt with an arc plasma between a tungsten electrode (cathode) and a water-cooled copper plate (anode). It is worth mentioning that Hsu and Pfender [6], in an attempt to check how close the electron temperature is to the temperature of the heavy particles and hence the validity of the assumption of local thermodynamic equilibrium, used a two-

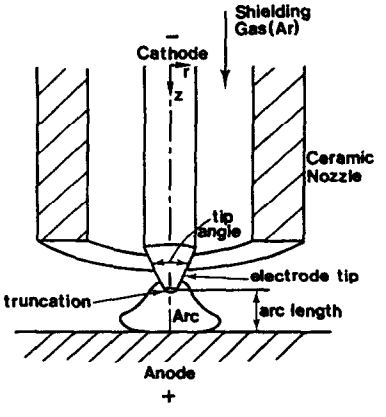

FIG. 1. Schematic sketch of the GTA welding process.

NOMENCLATURE

$\mathbf{B}$	magnetic field vector
B_θ	azimuthal component of magnetic field
C_p	specific heat
e	electron charge
$\mathbf{F}$	electromagnetic force per unit volume
h_1	metric coefficient for the η coordinate
h_2	metric coefficient for the ξ coordinate
H	enthalpy
I	arc current
$\mathbf{J}$	current density vector
j_η	η component of current density vector
j_ξ	ξ component of current density vector
J_t	current density along $\overline{BJ}$ (Fig. 2)
k	thermal conductivity
k_B	Boltzmann's constant
l	distance from point J along $\overline{JI}$ (Fig. 2)
L	length where j_η drops to zero along $\overline{JI}$ (equation (14))
p	pressure
r	radial distance
R_J	radial distance at point J
S_e	Joule heating caused by the arc resistance
S_R	optically thin radiation loss per unit volume
T	temperature
u	velocity component in the η-direction
w	velocity component in the ξ-direction
z	axial distance.

Greek symbols

ε	maximum allowable computational error
η	curvilinear coordinate
μ	viscosity of plasma
μ_0	magnetic permeability constant
ξ	curvilinear coordinate
ρ	density of plasma
σ	electrical conductivity of plasma
σ_{ij}	components of stress tensor
ϕ	any variable being computed.

temperature model to calculate heat transfer and fluid flow in the arc plasma. The results indicated that local thermodynamic equilibrium is a valid assumption in the arc plasma, especially in the region where the temperature is greater than about 10 000 K, and the ordinary one-temperature model approach [3] is accurate enough.

The use of an empirical heat transfer correlation in the study of McKelliget and Szekely [4] to account for convective heat transfer from the arc plasma to the anode is a very interesting approach for calculating the temperature distribution at the anode surface. While we are interested in exploring the application of this approach in the future, in the present study, we have used the measured plasma temperature distribution along the anode surface to test the validity of our model under more clearly defined conditions.

It should be emphasized, however, that practically all previous studies on heat transfer and fluid flow in the arc plasma, including those cited above [3–6], dealt with arcs significantly longer than those for practical GTA welding. For instance, the studies of Hsu and co-workers [3, 6] and McKelliget and Szekely [4] both dealt with 10 mm long arcs. In fact, it was not even arc welding that Hsu and co-workers [3, 6] intended to study. In the study of Kovitya and Cram [5], all arcs were 5 mm long, except for a 2 mm long 200 A arc. Obviously, GTAs under practical welding conditions deserve more attention, and this in fact is the main purpose of the present study.

It should also be emphasized that in the previous studies on heat transfer and fluid flow in the arc plasma, the electrode tip shape has been approximated either as a stepwise one [3, 6] or as a flat one [4]. The portion of the current entering the electrode tip through its conical surface and hence the electromagnetic force around that surface have not been calculated. While these assumptions might be reasonable in modeling long arcs like those studied by Hsu and co-workers [3, 6] and McKelliget and Szekely [4], they need to be released so that short arcs like those in practical GTA welding can be modeled properly. This is another main purpose of the present study.

Finally, since the shielding-gas nozzle is always used in GTA welding and yet it has not been considered in previous studies, it would be of practical interest to have it included in the model.

MATHEMATICAL FORMULATION

The cylindrical coordinates $[r, z]$ shown in Fig. 1 are transformed into axisymmetric orthogonal curvilinear coordinates $[\eta(r, z), \xi(r, z)]$, which fit the boundaries of the physical system, i.e. the cathode surface, the anode surface and the inner and bottom surfaces of the ceramic nozzle, as shown in Fig. 2. As a result of the use of these coordinates, the boundary conditions, especially those along the conical surface of the electrode tip, can be accurately described.

As in the previous studies [3–6], the flow is considered laminar in the present study. As explained by McKelliget and Szekely [4], the Reynolds number is of the order of 500. This is much lower than the Reynolds number of 100 000, around which the transition to turbulence in a free jet occurs.

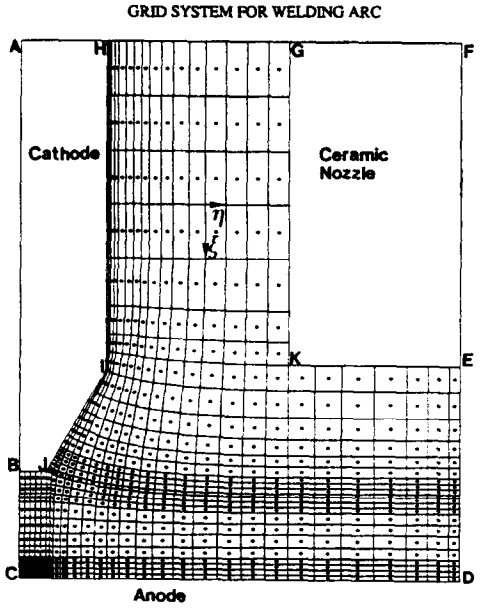

FIG. 2. The domain of calculation and the body-fitted orthogonal curvilinear coordinate system used for calculation.

The equation of continuity can be expressed as follows:

$$\frac{1}{h_1 h_2 r}\left[\frac{\partial}{\partial\eta}(h_2 r\rho u)+\frac{\partial}{\partial\xi}(h_1 r\rho w)\right]=0 \qquad (1)$$

where h_1 and h_2 are respectively the metric coefficients for the η and ξ coordinates, r the radial distance, u and w are respectively the velocity components in the η- and ξ-directions, and ρ the density.

The η and ξ components of the equation of motion are as follows [7]:

$$\begin{aligned}\frac{1}{h_1 h_2 r}\left[\frac{\partial}{\partial\eta}(\rho h_2 r u^2)+\frac{\partial}{\partial\xi}(\rho h_1 r u w)\right] &= -\frac{1}{h_1}\frac{\partial p}{\partial\eta}\\ &+\frac{1}{h_1 h_2 r}\left[\frac{\partial}{\partial\eta}(h_2 r\sigma_{11})+\frac{\partial}{\partial\xi}(h_1 r\sigma_{21})\right]\\ &+\frac{\sigma_{12}}{h_1 h_2}\frac{\partial h_1}{\partial\xi}-\frac{\sigma_{22}}{h_1 h_2}\frac{\partial h_2}{\partial\eta}+\frac{\rho w^2}{h_1 h_2}\frac{\partial h_2}{\partial\eta}\\ &-\frac{\rho u w}{h_1 h_2}\frac{\partial h_1}{\partial\xi}-\frac{\sigma_{33}}{h_1 r}\frac{\partial r}{\partial\eta}-j_\xi B_\theta \qquad (2)\end{aligned}$$

$$\begin{aligned}\frac{1}{h_1 h_2 r}\left[\frac{\partial}{\partial\eta}(\rho h_2 r u w)+\frac{\partial}{\partial\xi}(\rho h_1 r w^2)\right] &= -\frac{1}{h_2}\frac{\partial p}{\partial\xi}\\ &+\frac{1}{h_1 h_2 r}\left[\frac{\partial}{\partial\eta}(h_2 r\sigma_{12})+\frac{\partial}{\partial\xi}(h_1 r\sigma_{22})\right]\\ &+\frac{\sigma_{21}}{h_1 h_2}\frac{\partial h_2}{\partial\eta}-\frac{\sigma_{11}}{h_1 h_2}\frac{\partial h_1}{\partial\xi}+\frac{\rho u^2}{h_1 h_2}\frac{\partial h_1}{\partial\xi}\\ &-\frac{\rho u w}{h_1 h_2}\frac{\partial h_2}{\partial\eta}-\frac{\sigma_{33}}{h_2 r}\frac{\partial r}{\partial\xi}+j_\eta B_\theta \qquad (3)\end{aligned}$$

where the components of the stress tensor σ_{ij} are

$$\sigma_{11}=2\mu\left(\frac{1}{h_1}\frac{\partial u}{\partial\eta}+\frac{w}{h_1 h_2}\frac{\partial h_1}{\partial\xi}\right)-\tfrac{2}{3}\mu\frac{1}{h_1 h_2 r}\times\left[\frac{\partial}{\partial\eta}(h_2 r u)+\frac{\partial}{\partial\xi}(h_1 r w)\right] \qquad (4)$$

$$\sigma_{22}=2\mu\left(\frac{1}{h_2}\frac{\partial w}{\partial\xi}+\frac{u}{h_1 h_2}\frac{\partial h_2}{\partial\eta}\right)-\tfrac{2}{3}\mu\frac{1}{h_1 h_2 r}\times\left[\frac{\partial}{\partial\eta}(h_2 r u)+\frac{\partial}{\partial\xi}(h_1 r w)\right] \qquad (5)$$

$$\sigma_{33}=2\mu\left(\frac{u}{h_1 r}\frac{\partial r}{\partial\eta}+\frac{w}{h_2 r}\frac{\partial r}{\partial\xi}\right)-\tfrac{2}{3}\mu\frac{1}{h_1 h_2 r}\times\left[\frac{\partial}{\partial\eta}(h_2 r u)+\frac{\partial}{\partial\xi}(h_1 r w)\right] \qquad (6)$$

$$\sigma_{21}=\sigma_{12}=\mu\left[\frac{h_2}{h_1}\frac{\partial}{\partial\eta}\left(\frac{w}{h_2}\right)+\frac{h_1}{h_2}\frac{\partial}{\partial\xi}\left(\frac{u}{h_1}\right)\right]. \qquad (7)$$

In equations (2) and (3) j_η and j_ξ are respectively the η and ξ components of the current density vector **J**. and B_θ is the azimuthal (θ) component of the self-induced magnetic-field vector **B**. Also, $-j_\xi B_\theta$ and $j_\eta B_\theta$ are the η and ξ components of the electromagnetic force $F=\mathbf{J}\times\mathbf{B}$. The gravity force is negligible as compared to the electromagnetic force and is therefore neglected.

The equation of energy is as follows [3]:

$$\begin{aligned}\frac{1}{h_1 h_2 r}\left[\frac{\partial}{\partial\eta}(\rho h_2 r u H)+\frac{\partial}{\partial\xi}(\rho h_1 r w H)\right.&\\ =\left.\frac{1}{h_1 h_2 r}\left[\frac{\partial}{\partial\eta}\left(\frac{h_2 r}{h_1}\frac{k}{C_p}\frac{\partial H}{\partial\eta}\right)+\frac{\partial}{\partial\xi}\left(\frac{h_1 r}{h_2}\frac{k}{C_p}\frac{\partial H}{\partial\xi}\right)\right]\right.&\\ +S_J-S_R+S_e \qquad (8)&\end{aligned}$$

with

$$S_J=\frac{1}{\sigma}[j_\eta^2+j_\xi^2]$$

$$S_e=\frac{5}{2}\frac{k_B}{e}\left[\frac{j_\eta}{C_p h_1}\frac{\partial H}{\partial\eta}+\frac{j_\xi}{C_p h_2}\frac{\partial H}{\partial\xi}\right].$$

In the above equations H is the enthalpy, k the thermal conductivity, C_p the specific heat, k_B the Boltzmann constant, e the elementary charge and σ the electrical conductivity. S_J represents the Joule heating caused by the arc resistance, S_R the optically thin radiation loss per unit volume, and S_e represents the transport of electron enthalpy due to the fact that the electron velocity is generally much higher than the heavy particle velocity. The radiation loss was taken from the study of Evans and Tankin [8], and the remaining plasma properties from the tabulated data of Liu [9].

It should be mentioned that in the data of Liu [9], the argon plasma properties are given (in the form of a table) as a function of temperature, including the

viscosity μ, density ρ, thermal conductivity k, specific heat C_p and electrical conductivity σ. These properties are given at 1 atm pressure, i.e. the welding pressure. The calculated results of ours and others (e.g. ref. [3]) showed that the pressures in the arc deviate by less than or around 1% from 1 atm pressure. As such, the effect of variations in pressure on the physical properties can be neglected.

In order to calculate the electromagnetic field, Maxwell's equations need to be solved. In the studies of Hsu *et al.* [3], this was achieved by first calculating the electric potential field, then calculating the current density vector from the potential field using Ohm's law, and finally calculating the self-induced magnetic field B_θ using relationships equivalent to the following ones:

$$\mu_0 j_\xi = \frac{1}{r}\frac{\partial}{h_1 \partial \eta}(rB_\theta) \tag{9}$$

$$-\mu_0 j_\eta = \frac{1}{r}\frac{\partial}{h_2 \partial \xi}(rB_\theta) \tag{10}$$

where μ_0 is the magnetic permeability constant.

In the study of McKelliget and Szekely [4], on the other hand, the self-induced magnetic field B_θ was calculated using a 'magnetic diffusion equation' equivalent to the following one:

$$\frac{\partial}{\partial \xi}\left[\frac{1}{\sigma r}\frac{h_1}{h_2}\frac{\partial}{\partial \xi}(rB_\theta)\right] + \frac{\partial}{\partial \eta}\left[\frac{1}{\sigma r}\frac{h_2}{h_1}\frac{\partial}{\partial \eta}(rB_\theta)\right] = 0. \tag{11}$$

The current density vector was then calculated from the self-induced magnetic field B_θ using relationships equivalent to equations (9) and (10). We have tried both approaches and, since they are equivalent to each other in principle, we have come up with essentially identical results. However, we feel that the approach based on equations (9)–(11) is more convenient to use and have, therefore, decided to adopt it in the present study. The approach of Hsu *et al.* [3], however, has the advantage that other mechanisms which may drive the current can be easily incorporated (i.e. diffusion and thermal diffusion). These effects may become very important close to the electrodes, where strong axial gradients exist.

The domain of calculation and the boundary conditions are specified with reference to Fig. 2 and Table 1. The dimensions for boundaries AC and CD are 10 and 8.2 mm, respectively. In brief, the velocity boundary condition along HG is the equation given by Bird *et al.* [10] for laminar flow through an annulus. The boundary condition along ED is based on the negligible axial velocity component and the equation of continuity, i.e. equation (1). The remaining velocity boundary conditions express the no-slip condition at solid surfaces and the zero-flux condition across the axis of symmetry. The thermal boundary conditions express the reported electrode temperature distributions along surfaces JI and IH [11], plasma temperature distributions along the lower end of the electrode tip BJ [5] and the anode surface CD [12], and gas temperature along the outlet ED [3, 4]. They also express the zero-flux condition across the axis of symmetry, and across the inner and bottom walls of the ceramic nozzle. It should be emphasized that the domain of the temperature calculation, as in the previous studies [3–6], does not include the sheaths.

The magnetic-field boundary conditions can be classified into two different groups according to whether or not the current density vector is specified. In the first group, the current density vector is specified along the following boundaries:

$$j_\eta = 0 \text{ along } \overline{CD} \text{ and } \overline{BC} \tag{12}$$

$$j_\xi = J_t \text{ along } \overline{BJ} \tag{13}$$

$$j_\eta = J_t(1 - l/L) \text{ along } \overline{JI} \tag{14}$$

with

$$\int_0^{R_J} 2\pi r j_\xi \, dr + \int_0^L 2\pi r j_\eta \, dl = I$$

where J_t is the current density at the end of the electrode tip, l the distance from point J along JI; j_η drops to zero at $l = L$, R_J is the radius at point J and I the welding current. In the above expressions, the first one is based on the physical requirement of zero flux across the axis of symmetry and tangent to the anode surface. The remaining two, however, represent a simple approximation for the current density distribution along the electrode tip, the actual information of which unfortunately is currently unavailable—the approximate current density distribution of Cram [13] for a 100 A arc is not applicable to the 200 A arcs being studied here. With the help of equations (9) and (10), the above three expressions for the current density vector can be used to deduce the boundary conditions for the self-induced magnetic field B_θ along the anode surface, the axis of symmetry and the electrode tip. In the second group of boundary conditions, on the other hand, Ampere's law is used, i.e.

$$B_\theta = \frac{\mu_0 I}{2\pi r}. \tag{15}$$

METHOD OF SOLUTION

The orthogonal curvilinear coordinates in Fig. 2 were generated numerically by solving coordinate transformation equations [14]. For better accuracy, the coordinate lines are more closely spaced near the electrode, the axis of symmetry and the anode, where steeper gradients of field variables are expected. Further grid refinement did not result in significant changes in the calculated results. As shown, the grid system is staggered, with components of the vector variables (e.g. velocity, current density vector and magnetic field vector) being evaluated at mid points of the line segments (representing the cell surfaces)

Table 1. Boundary conditions

	u	w	H or T	B_θ
$\overline{BC}$	0	$\partial w/\partial\eta = 0$	$\partial H/\partial\eta = 0$	0
$\overline{CD}$	0	0	H_{exp}	$\partial(rB_\theta)/\partial\xi = 0$
$\overline{ED}$	$\partial(h_2 r\rho u)/\partial\eta = 0$	0	1000 K	equation (15)
$\overline{KE}$	0	0	$\partial H/\partial\xi = 0$	equation (15)
$\overline{GK}$	0	0	$\partial H/\partial\eta = 0$	equation (15)
$\overline{HG}$	0	equation (2.4–13) in ref. [10]	$\partial H/\partial\xi = 0$	equation (15)
$\overline{HI}$	0	0	H_{exp}†	equation (15)
$\overline{IJ}$	0	0	H_{exp}†	equations (9) and (14)
$\overline{BJ}$	0	0	20000 K	equations (10) and (13)

† The electrode surface temperature decreases linearly with decreasing z from 3200 K at point J to 2700 K at point H [11].

and the scalar variables (e.g. temperature and pressure) at the positions of the dots (representing the cell centers). The resultant vectors, however, are still plotted at the positions of the dots. Staggered grids have been widely used in fluid flow calculations based on primitive variables [15].

Equations (1)–(7) were solved using a finite-volume method based on the SIMPLE algorithm and the power-law scheme [15]. Calculations were carried out in the physical domain. Weighted (i.e. based on the lever-arm-rule), rather than central, three-point differencing was used to minimize errors caused by non-uniform grid spacing. Since both the finite-volume method and weighted differencing are used, second-order accuracy is still obtained even with the use of non-uniform grid spacing. A detailed description of the discretization scheme, which is too lengthy to present here, has been given by Patankar [15].

The convergence criteria are as follows:

$$\left|\frac{\partial r}{\partial\eta}\frac{\partial r}{\partial\xi} + \frac{\partial z}{\partial\eta}\frac{\partial z}{\partial\xi}\right|_{max} \leqslant 10^{-6}$$

for the orthogonality requirement of the grid system, and

$$\frac{\sum|\phi^{new} - \phi^{old}|}{\sum|\phi^{new}|} \leqslant \varepsilon$$

for variables being computed where Σ denotes summation over all grid points, max denotes the maximum value of all grid points, and ϕ denotes one of the variables being evaluated. The values of ε are 10^{-5} for the self-induced magnetic field B_θ, and 10^{-3} for other variables such as enthalpy, velocities, and pressure.

RESULTS AND DISCUSSION

The spectroscopic temperature measurement of Haddad and Farmer [12] for a 2 mm long 200 A GTA appears to be the only source of experimental data known to us as being relevant to practical GTA welding conditions. For the purpose of comparison, we have conducted the heat transfer and fluid flow calculation based on their experimental condition. In brief, the electrode radius is 1.6 mm, the angle of the electrode tip is 60° (i.e. the angle between the extensions of AB and IJ in Fig. 2 is 30°), the inner radius of the ceramic nozzle is 5 mm, the wall thickness of the nozzle is 3.2 mm, and the flow rate of pure argon is 10 l min^{-1}.

Current density and electromagnetic force

Regarding the current density distribution at the electrode tip, i.e. equations (13) and (14), we specified $J_t = 0.7 \times 10^8$ A m^{-2} and $L = 1.0$ mm. This value of J_t, as will be described later, is close to those used in previous studies. From these values, a 0.5 mm radius at the lower end of the electrode tip (i.e. BJ = 0.5 mm in Fig. 2) is obtained. Although no electrode tip truncation was mentioned in the study of Haddad and Farmer [12], the apex of a sharpened and untruncated electrode usually tends to experience some melting and rounding up, and the 0.5 mm radius does not seem unreasonable. The amounts of current entering the lower end and the conical surface of the electrode tip are thus 53 and 147 A, respectively. It is interesting to note that the maximum current density of 0.7×10^8 A m^{-2} and the cathode spot radius of 1.0 mm (0.5 mm + 1.0 mm × sin 30°) fall within the ranges adopted in previous studies [3–6], i.e. a maximum current density from 0.65×10^8 to 1.20×10^8 A m^{-2} and a cathode spot radius of 0.45–1.0 mm.

The calculated current density distribution in the arc plasma is shown in Fig. 3 (the current density vectors smaller than 0.2×10^8 A m^{-2} in magnitude are omitted). As shown, the welding current leaves the anode surface and enters the electrode tip through the cathode spot. The current density at the anode is on the average less than that at the cathode spot, due to the smaller area of the latter. The current density vector, when integrated over the anode surface, yields a total current within 0.1% error of the welding current. We have found this a useful check on the accuracy of current-density calculation. It should be pointed out that, although all the current-density vectors near the anode surface appear to be perpendicular

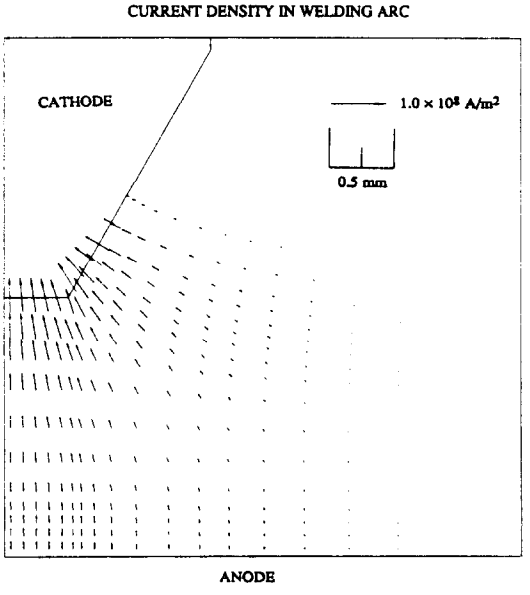

FIG. 3. Calculated current density distribution for a sharpened electrode.

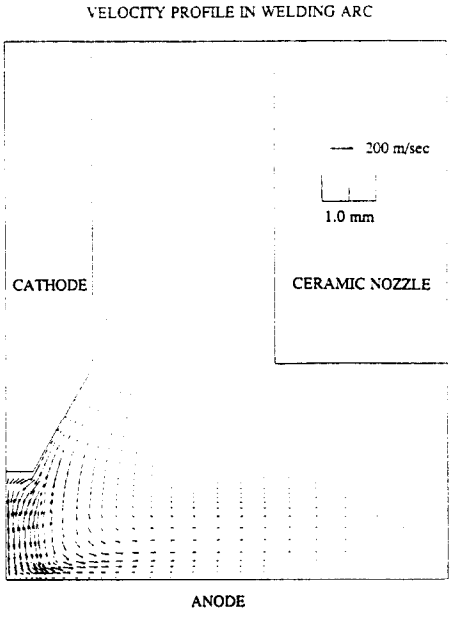

FIG. 5. Calculated velocity distribution for a sharpened electrode.

to it, the same does not seem true near the cathode surface. This is because these vectors are located not exactly at the electrode-tip surface, but at the dots slightly off it (see Fig. 2). The tangential components of the current density vectors at the electrode-tip surface are indeed zero, as required by the specified current density distribution at the electrode tip.

Figure 4 shows the calculated distribution of the electromagnetic force in the arc plasma (the vectors less than 0.1×10^6 N m^{-3} in magnitude are omitted). As shown, the electromagnetic force is very small near the lower portion of the axis of symmetry, where the self-induced magnetic field approaches zero, and in the outer portion of the arc plasma near the anode surface, where the current density is very small. On the other hand, the electromagnetic force is more significant right below the lower end of the electrode tip, where the current density is rather strong (see Fig. 4). This inward and slightly downward electromagnetic force and the zero-flux condition across the axis of symmetry cause a downward fluid flow along the axis of symmetry and toward the anode. More importantly, the electromagnetic force adjacent to the lower portion of the conical surface of the electrode tip is rather strong. This electromagnetic force, which has not been calculated in previous studies [3–6], tends to push the adjacent fluid downward and inward, producing a significant effect on both the velocity and temperature fields in the arc plasma, as will be described below.

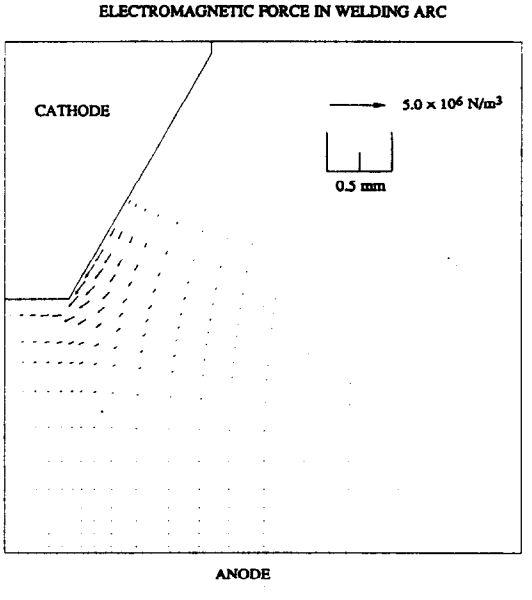

FIG. 4. Calculated electromagnetic force distribution for a sharpened electrode.

Velocity

The calculated velocity distribution in the arc plasma and the shielding gas is shown in Fig. 5. As shown, in the region directly under the lower end of the electrode tip, the fluid flows downward along the axis of symmetry. Due to the stagnation effect at the anode the fluid is then deflected and flows radially outward. The maximum velocity in the arc plasma is near the mid point of the axis of symmetry, and is 206 m s^{-1}. Beyond this region, i.e. in the region of the arc plasma under the conical surface of the electrode tip, the fluid first flows inward and downward and then, as it approaches the anode, it turns radially outward, again due to the stagnation effect. As a result of the impingement of the high-velocity heavy particles, the anode surface is subjected to the so-called arc

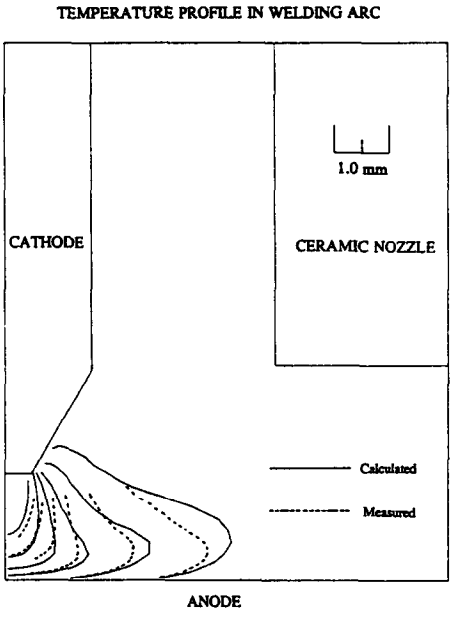

FIG. 6. Calculated temperature distribution for a sharpened electrode. The measured temperature distribution of Haddad and Farmer [12] are included for comparison. The isotherms from right to left are 11 000, 13 000, 15 000, 17 000, 19 000 and 21 000 K.

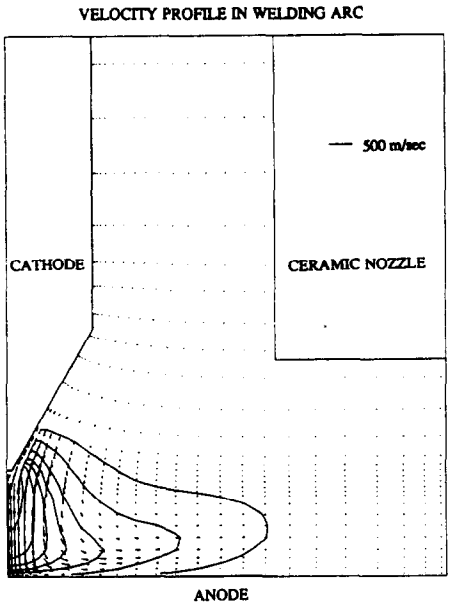

FIG. 7. Calculated velocity and temperature distributions for a sharpened electrode which has the same included angle of the electrode tip as that in Figs. 5 and 6, but with a greater portion of the welding current entering the inclined surface of the electrode.

pressure. The calculated maximum arc pressure, which is located at the axis of symmetry at the anode surface, is 753 N m^{-2}. This compares well with the measured value of about 830 N m^{-2} by Yamauchi and Taka [16] for a similar arc. From Fig. 5 the presence of the ceramic nozzle, at least in the present case, does not seem to have a pronounced effect on the velocity distribution in the arc plasma. The fluid flow near the electrode surface first increases as the upper end of the inclined surface is approached and then decreases beyond that point. This is because of the area available for flow expands due to the decreasing cross-sectional area of the electrode. As shown in Fig. 5, the inlet and outlet velocities of the fluid are much smaller than the velocities in the arc plasma. As such, the boundary conditions for the inlet and outlet velocity distributions do not actually have a significant effect on the velocity distribution in the arc plasma.

Temperature

Figure 6 shows the calculated temperature distribution in the arc plasma. The isotherm of 11 000 K provides a rough estimation of the arc periphery. The maximum temperature is about 23 000 K and is located at the axis of symmetry near the lower end of the electrode tip. The previously mentioned strong radially outward flow of the fluid (Fig. 5), which is promoted by the downward and inward electromagnetic force near the lower portion of the inclined surface, has caused the formation of a bell-shaped arc. The width/height ratio of this bell-shaped arc is much larger than those of long arcs [3–6]. Such a bell-shaped arc is often observed in GTA welding, especially with an electrode tip angle around or less than 60° [16]. The measured temperature distribution of Haddad and Farmer [12] is included in the figure for comparison. As shown, the agreement is good for temperatures down to about 13 000 K. However, the calculated isotherm for the temperature of 11 000 K, where the local thermodynamic equilibrium assumption may not be as valid as at higher temperatures, deviates significantly from the observed one.

The calculated temperature distribution in the arc plasma is not very sensitive to the temperature boundary conditions at the top (HG), the outlet (ED) and the electrode surface (HI), since the fluids at these boundaries are much cooler than the arc plasma. In fact, the calculated temperature distribution is not very sensitive to the temperature boundary condition at the anode surface (CD) either, due to the fact that the plasma temperature drops rather rapidly immediately adjacent to the anode surface.

On the other hand, heat transfer and fluid flow in the arc plasma are rather sensitive to the amount and distribution of current along the conical surface of the electrode tip. To illustrate this, we have assigned $J_t = 1.98 \times 10^8$ A m^{-2} and $L = 1.1$ mm, which correspond to allocating a 6.2 A current to a 0.1 mm radius lower end of the electrode tip (i.e. BJ = 0.1 mm) and a 193.8 A current to the conical surface. This results in an electromagnetic force field adjacent to the inclined surface of the electrode tip significantly stronger than that previously shown in Fig. 4. As shown in Fig. 7, the velocities in the arc plasma are

significantly higher than those shown previously in Fig. 5, the maximum now being 484 m s^{-1} and located not along the axis of symmetry any more, but about 0.23 mm away from it. As a result of this significantly stronger velocity field, the maximum arc pressure at the anode surface is much higher, being around 2000 N m^{-2}, and the isotherms are pushed further outward (compare with Fig. 6).

Effects of electrode-tip geometry

In order to illustrate the effects of the electrode-tip geometry, an electrode with a flat end, i.e. with a tip angle of 180°, was considered. The current and the arc length were still 200 A and 2 mm, respectively. In view of the fact that the cathode spot in a flat-ended electrode tends to move around rather randomly and quickly, a time-averaged radius of 1.2 mm was assigned to the cathode spot, with a uniform current density of 0.44×10^8 A m^{-2}. The boundary conditions were equivalent to those shown in Table 1 for the previous case (with BJ now being 1.2 mm). It is recognized that the temperature distribution of the plasma along the anode surface, i.e. the temperature boundary condition at CD, is no longer the same as that in the previous case. However, due to the lack of experimental data for the present case and in view of the fact that the calculated temperature distribution in the arc plasma is not very sensitive to it, this boundary condition was kept the same.

The calculated current density and electromagnetic force distributions are shown in Figs. 8 and 9. As compared with those shown in Figs. 3 and 4 for the previous case, on the average the current density vectors here are more nearly parallel to the axis of symmetry while the electromagnetic force vectors are more nearly perpendicular to it.

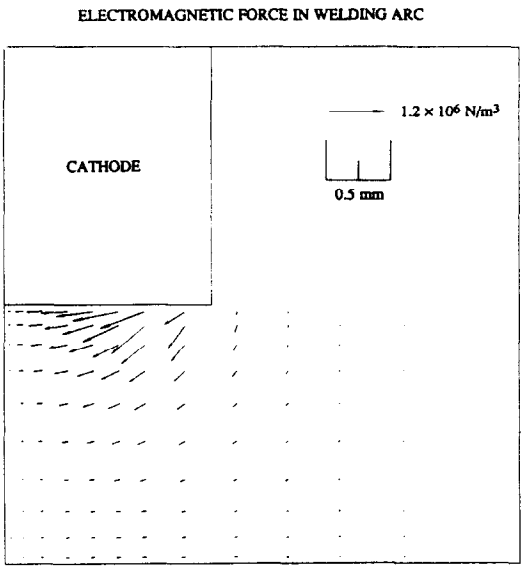

FIG. 9. Calculated electromagnetic force for a flat electrode.

The calculated velocity and temperature distributions are shown in Figs. 10 and 11. The maximum velocity and temperature are around 170 m s^{-1} and 23 000 K, respectively. As compared with those shown in Figs. 5 and 6 for the previous case, the radially outward flow of the fluid is less significant and the arc periphery is no longer bell-shaped. This change in the arc shape with the change in the electrode-tip

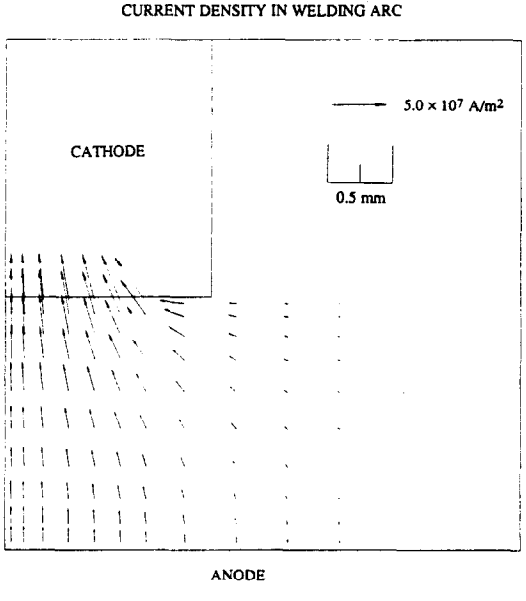

FIG. 8. Calculated current density distribution for a flat electrode.

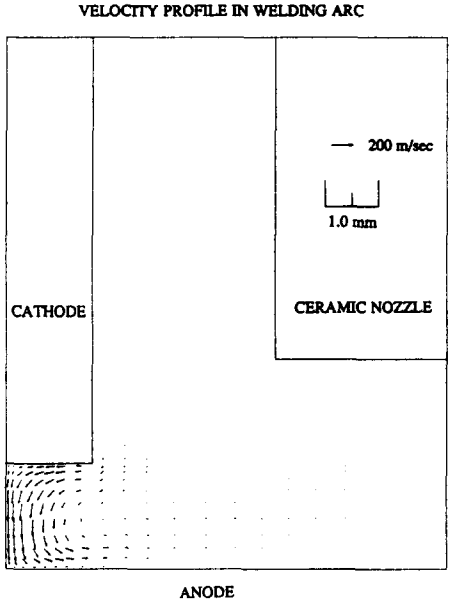

FIG. 10. Calculated velocity distribution for a flat electrode.

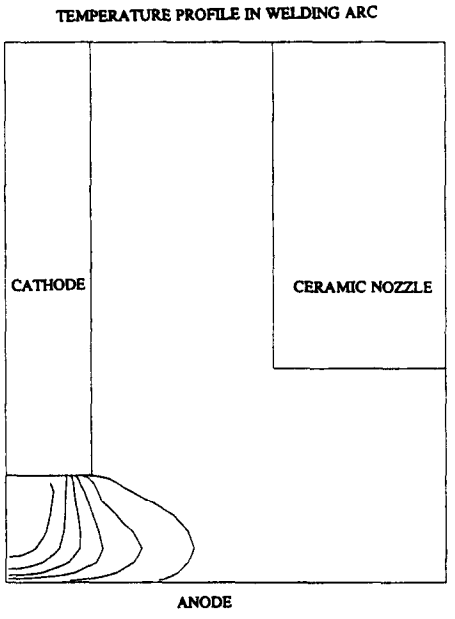

FIG. 11. Calculated temperature distribution for a flat electrode. The isotherms from right to left are 11 000, 13 000, 15 000, 17 000, 19 000 and 21 000 K.

geometry is consistent with experimental observations [17]. It is interesting to note that the maximum arc pressure at the anode surface, 585 N m^{-2}, is lower than that in the previous case, due to the lower downward velocities of the fluid in the present case. This decrease in the maximum arc pressure with increasing electrode tip angle is also consistent with experimental observations [16].

CONCLUSIONS

(1) A steady-state, two-dimensional model has been developed to describe heat transfer and fluid flow in gas-tungsten welding arcs. This model differs from the previous ones in that it considers the electrode tip geometry, the arc length realistic for welding and the presence of the shielding-gas nozzle.

(2) The portion of the welding current entering the conical surface of the electrode tip tends to create an electromagnetic force parallel to the conical surface, pushing downward and inward the fluid surrounding that surface and promoting the formation of a bell-shaped welding arc. Heat transfer and fluid flow in the arc plasma are rather sensitive to the distribution of current along the electrode tip.

(3) The calculated temperature distribution in the arc plasma, especially in the region above 13 000 K, and the calculated maximum arc pressure at the anode surface both agree well with existing experimental data.

(4) The effects of the electrode tip geometry, on the arc shape and the maximum arc pressure at the anode surface, described by the present model are consistent with experimental observations.

(5) The presence of the shielding-gas nozzle, at least under the conditions of the present study, does not seem to have a significant effect on the velocity and temperature distributions in the arc plasma.

Acknowledgements—This study was supported by the National Science Foundation under DMR 8419274 and by the Graduate School of the University of Wisconsin. One of the authors (S. Kou) would like to thank Professor E. Pfender for helpful discussions.

REFERENCES

1. *Welding Handbook* (7th Edn), Vol. 2, p. 77. American Welding Society, Miami, Florida (1978).
2. S. Kou and Y. H. Wang, Weld pool convection and its effect, *Welding J.* **65**, 63–70s (1986).
3. K. C. Hsu, K. Etemadi and E. Pfender, Study of the free-burning high-intensity argonarc, *J. Appl. Phys.* **54**, 1293–1301 (1983).
4. J. McKelliget and J. Szekely, Heat transfer and fluid flow in the welding arc, *Metall. Trans.* **17A**, 1139–1148 (1986).
5. P. Kovitya and L. E. Cram, A two-dimensional model of gas-tungsten welding arcs, *Welding J.* **65**, 34–39s (1986).
6. K. C. Hsu and E. Pfender, Two-temperature modeling of the free-burning, high-intensity arc, *J. Appl. Phys.* **54**, 4359–4366 (1983).
7. L. E. Malvern, *Introduction to the Mechanics of a Continuous Medium*, pp. 641–672. Prentice-Hall, New York (1969).
8. D. L. Evans and R. S. Tankin, Measurement of emission and absorption of radiation by an argon plasma, *Physics Fluids* **10**, 1137–1144 (1967).
9. C. H. Liu, Numerical analysis of the anode region of high intensity arcs, Ph.D. Thesis, University of Minnesota (1977).
10. R. B. Bird, W. E. Stewart and E. N. Lightfoot, *Transport Phenomena*, p. 53. Wiley, New York (1960).
11. W. F. Savage, S. S. Strunck and Y. Ishikawa, The effect of electrode geometry in gas tungsten-arc welding, *Welding J.* **44**, 489–496s (1965).
12. G. N. Haddad and A. J. D. Farmer, Temperature measurements in gas tungsten arcs, *Welding J.* **64**, 339–342s (1985).
13. L. E. Cram, A model of the cathode of a thermoionic arc, *J. Phys. D: Appl. Phys.* **16**, 1643–1650 (1983).
14. A. Thom and C. J. Apelt, *Field Computation in Engineering and Physics*, p. 130. Van Nostrand, London (1961).
15. S. V. Patankar, *Numerical Heat Transfer and Fluid Flow*, Chaps 5 and 6. Hemisphere, Washington, DC (1980).
16. N. Yamauchi and T. Taka, TIG arc welding with hollow tungsten electrode, IIW Document 212 G-452-79, International Welding Institute, London (1979).
17. S. S. Glickstein, Basic studies of the arc welding processes. In *Trends in Welding Research in the United States* (Edited by S. A. David), pp. 3–51. American Society for Metals, Metals Park, Ohio (1982).

TRANSFERT THERMIQUE ET ECOULEMENT DANS DES ARCS DE SOUDAGE PRODUITS PAR DES ELECTRODES POINTUES OU PLATES

Résumé—Un modèle bidimensionnel permanent est développé pour décrire le transfert thermique et l'écoulement dans des arcs de soudage à tungstène gazeux. Le modèle diffère des autres parce qu'il considère la géométrie de l'extrémité de l'électrode, la longueur d'arc réaliste pour le soudage et la présence d'une couverture gazeuse au nez. Les effets de la géométrie de l'extrémité sont démontrés, par le modèle, s'exercer sur les points suivants; la distribution de la densité de courant, la force électromagnétique, la vitesse et la température du plasma d'arc, la forme de l'arc et la pression d'arc. La distribution de température calculée et la pression maximale d'arc sont comparées avec des données expérimentales.

WÄRMEÜBERTRAGUNG UND STRÖMUNG IN EINEM SCHWEISS-LICHTBOGEN BEI VERWENDUNG SPITZER UND STUMPFER ELEKTRODEN

Zusammenfassung—Ein zweidimensionales stationäres Modell zur Beschreibung der Wärmeübertragung und Strömung in Gas-Wolfram-Schweißlichtbögen wird entwickelt. Das Modell unterscheidet sich von bisherigen Modellen dadurch, daß es die Geometrie der Elektrodenspitze, eine für Schweißvorgänge realistische Lichtbogenlänge und die Gegenwart der Schutzgasdüse berücksichtigt. Der Einfluß der Geometrie der Elektrodenspitze auf die folgenden Prozeßparameter wird mit dem Modell untersucht: die Verteilungen der Stromdichte, der elektromagnetischen Kräfte, der Strömungsgeschwindigkeit und der Temperaturen im Lichtbogenplasma, außerdem die Form des Lichtbogens und der Druck. Die berechnete Temperaturverteilung im Lichtbogenplasma und der maximale Druck im Lichtbogen an der Anode werden mit bekannten experimentellen Ergebnissen verglichen.

ТЕПЛОПЕРЕНОС И ТЕЧЕНИЕ ЖИДКОСТИ В СВАРОЧНЫХ ДУГАХ, ОБРАЗОВАННЫХ ЗАОСТРЕННЫМИ И ПЛОСКИМИ ЭЛЕКТРОДАМИ

Аннотация—Разработана стационарная двумерная модель для описания теплопереноса и газодинамика в сварочных дугах с вольфрамовым катодом. В отличие от предыдущих, данная модель учитывает геометрию острия электрода, реальную длину сварочной дуги, а также наличие насадки для подачи защитного газа. С использованием указанной модели демонстрируется влияние геометрии острия электрода на следующие параметры: распределения плотности тока, электромагнитной силы, скорости и температуры дуговой плазмы, а также на форму дуги и давление. Рассчитанные температурные распределения в дуговой плазме и максимальное давление в дуге у анода сравниваются с имеющимися экспериментальными данными.